Title: Assessment of the sources of error affecting the quantitative accuracy of SPECT imaging in small animals

Authors: Andrew B. Hwang[1,2], Benjamin L. Franc[1,2], Grant T. Gullberg[1,2,3], Bruce H. Hasegawa[1,2]

Affiliations:

[1] Joint Graduate Group in Bioengineering, University of California, San Francisco, and University of California, Berkeley. 1700 4th Street, MC0775, San Francisco, CA 94158-2330.

[2] Department of Radiology, University of California, Campus Box 0628, San Francisco, San Francisco, CA 94143-0628

[3] Lawrence Berkeley National Laboratory, 1 Cyclotron Road, Mail Stop 55R0121, Berkeley, CA 94720-8119

Keywords: Single photon emission computed tomography (SPECT), SPECT/CT, quantitative measurements and scanning

Abstract

Small animal SPECT imaging systems have multiple potential applications in biomedical research. Whereas SPECT data commonly are interpreted qualitatively in a clinical setting, the ability to accurately quantify measurements will increase the utility of the SPECT data for laboratory measurements involving small animals. In this work, we assess the effect of photon attenuation, scatter, and partial volume errors on the quantitative accuracy of small animal SPECT measurements, first with Monte Carlo simulation and then confirmed with experimental measurements. The simulations modeled the imaging geometry of a commercially available small animal SPECT system. We simulated the imaging of a radioactive source within a cylinder of water, and reconstructed the projection data using iterative reconstruction algorithms. The size of the source and the size of the surrounding cylinder were varied to evaluate the effects of photon attenuation and scatter on quantitative accuracy. We found that photon attenuation can reduce the measured concentration of radioactivity in a volume of interest in the center of a rat

sized cylinder of water by up to 50% when imaging iodine-125, and up to 25% when imaging

technetium-99m. When imaging with iodine-125, the scatter-to-primary ratio can reach up to

approximately 30%, and can cause overestimation of the radioactivity concentration when

30   reconstructing data with attenuation correction. We varied the size of the source to evaluate

partial volume errors, which we found to be a strong function of the size of the volume of

interest and the spatial resolution. These errors can result in large (>50%) changes in the

measured amount of radioactivity. The simulation results were compared with, and found to

agree with experimental measurements. The inclusion of attenuation correction in the

35   reconstruction algorithm improved quantitative accuracy. We also found that improvement of

the spatial resolution through the use of resolution recovery techniques (*i.e.*, modeling the finite

collimator spatial resolution in iterative reconstruction algorithms) can significantly reduce the

partial volume errors.

I. INTRODUCTION

40   Small animal SPECT imaging has many applications for the *in vivo* assessment of

physiological function in basic biological research and drug development (Booij, de Bruin *et al*.

2002; Bennink, Hamann *et al*. 2005; Meikle, Kench *et al*. 2005; Zhou, Thomas *et al*. 2005).

However, the scientific utility of these data are increased when they are analyzed and recorded

quantitatively. In fact, various approaches have been developed to analyze nuclear medicine

45   data in a quantitative manner. For example, the regional uptake of radiopharmaceuticals such as

^{99m}Tc-sestamibi is often compared against a database to quantify the severity of myocardial

perfusion defects in patients with coronary artery disease.

The term "radionuclide quantification" has several different meanings in the medical imaging

literature.   Definitions include: 1) "semiquantification", the comparison of relative

50   measurements between normal and diseased regions, 2) "physiologic quantification", the

measurement of a physiological parameter (*e.g.*, rate of perfusion), and 3) "absolute physical

quantification", the accurate measurement of radioactivity concentration (in physical units of

MBq/ml) (Van Laere and Zaidi 2006). Within this manuscript, radionuclide quantification is

used to describe absolute physical quantification, the measurement of the absolute concentration

55   of radiotracer within a volume of interest (VOI).

      Quantitative measurement of radioactivity uptake using SPECT is hampered by a number of

physical perturbations, namely photon attenuation, photon scatter, and partial volume errors.

Photon attenuation is caused by interactions between emitted photons and the surrounding

tissues, which reduce the number of photons incident upon the detector and result in a reduction

60   in the measured radioactivity. The magnitude of this effect is related to the energy of the emitted

photon, and the amount and type of overlying tissue. Likewise, scatter results from the

interactions of emitted photons with the surrounding tissue, resulting in a change in the photon's

energy and trajectory. This changes the apparent source of the photon and affects the image

contrast, although some scattered photons can be rejected by energy discrimination. Partial

65   volume errors arise from the limited spatial resolution of radionuclide imaging systems which

causes "spill-out" of activity from a VOI and thereby decreases the measured concentration of

radioactivity. Partial volume errors also can cause "spill-in" of activity from structures adjacent

to the VOI. These phenomena occur in all forms of radionuclide imaging, but have different

magnitudes in small animal imaging in comparison to clinical imaging.

70   The objective of this work is to estimate the magnitude of the above discussed perturbations

in small animal SPECT, errors that may be expected in the quantification of radiotracers. We

also show that iterative image reconstruction algorithms can be used to improve quantitative

accuracy by compensating for these errors.

II.   MATERIALS AND METHODS

75   In order to assess the quantitative accuracy of small animal SPECT imaging, we performed

Monte Carlo simulations and experimental measurements to estimate the effect of various

perturbations on the quantitative accuracy of SPECT imaging.   We used Monte Carlo

simulations to generate projection data for a spherical source of radioactivity to assess the effects

of photon attenuation, scatter, and partial volume errors.   The data were then reconstructed using

80   iterative reconstruction algorithms designed to compensate for various effects, including photon

attenuation correction and collimator response modeling.   The concentration of radioactivity in

the VOI was then measured.   We also performed experimental phantom measurements using a

commercially available small animal SPECT/CT scanner (X-SPECT®, Gamma Medica-Ideas,

Inc., Northridge, CA)

85   **A.   X-SPECT scanner**

The X-SPECT scanner is a dedicated small animal SPECT/CT imaging system.   The SPECT

imaging component of this system is based on a gamma camera using a segmented NaI(Tl)

scintillator coupled to position sensitive photomultiplier tubes.   The detector of the system used

in this study has 54×54 pixels, with a pitch of 2.2 mm.   The energy resolution of the detector at

90   140 keV is approximately 11% full-width-at-half-maximum (McElroy, MacDonald *et al*. 2002).

For this study, imaging was performed with a pinhole collimator having a focal length of 9 cm

and pinhole apertures of 1 mm or 2 mm diameter.   The spatial resolution was assessed for planar

imaging using a line source filled with technetium-99m placed 4 cm from the pinhole and was

determined to be 1.6±0.1 mm full-width half-maximum (FWHM) and 2.5±0.1 mm FWHM for

95   the 1 mm and 2 mm pinhole apertures, respectively (Hwang 2006).   Although the X-SPECT can

be equipped with two gamma cameras, we used a system with only one detector. However, the methods and results of this study are generally applicable to SPECT systems with multiple heads.

The X-SPECT scanner uses a microfocus x-ray tube and a CMOS based detector to perform x-ray CT imaging. The x-ray tube has a fixed tungsten anode and produces a maximum tube current of 1 mA at 50 kVp with a nominal focal spot size of 100 μm. The detector has 2368×2240 pixels with a nominal pixel pitch of 50 μm. All experimental imaging studies were performed with this SPECT/CT system.

B.   Monte Carlo simulations

Monte Carlo methods are powerful tools for simulating a variety of physical processes and are often used to model radionuclide imaging systems. Monte Carlo simulations are particularly useful for studying quantitative measurements in SPECT because it becomes possible to simulate the imaging of a well defined radionuclide source while modeling complex physical phenomena such as photon scatter. The simulations in this work modeled physical effects including Compton scatter, coherent (Rayleigh) scatter, and photoelectric absorption, and were performed using GATE ("Geant4 Application for Tomographic Emission"), which is based on the Geant4 Monte Carlo package (Agostinelli, Allison *et al*. 2003; Santin, Strul *et al*. 2003; Strul, Santin *et al*. 2003; Allison, Amako *et al*. 2006). The simulation geometry assumed a simplified model of the X-SPECT scanner (Figure 1) having a simplified pinhole collimator created by simulating a round sheet of tungsten with a keel edge pinhole aperture in the center. The detector was modeled as a single $12 \times 12 \text{ cm}^2$ piece of NaI(Tl) scintillator encased in lead shielding positioned 9 cm from the pinhole center. The radius of rotation was 4 cm for all simulations. Blurring within the detector crystal was not modeled, but the projection data were read out in a 54×54

format, giving an effective pixel size of 2.2 mm. The simulated detector energy resolution and

120   energy windows are shown in Table 1. The energy resolution was based on published

information about the detector (McElroy, MacDonald *et al.* 2002), and the energy windows were

based on the settings that we use experimentally. The objective of these simulations was to

estimate the effects of photon attenuation, photon scatter, and partial volume errors.

To study the effect of attenuation and scatter, the simulation modeled a spherical source of

125   radioactivity with a radius of 2 mm positioned at the isocenter of the imaging system. The

photons had a simulated energy of 27.5 keV to model the imaging of iodine-125. The source

was first simulated in air. The simulation was then performed with the source located at the

center of a cylinder of water having a height of 3 cm and a radius varying from 0.5 cm and 2.5

cm to assess the effect of different levels of attenuation and scatter. For each cylinder radius, 64

130   projections were simulated with 1.5×10^6 photons per projection. The simulations modeled

imaging using a 2 mm pinhole aperture (the 1 mm pinhole was not simulated because the effects

of attenuation and scatter are expected to be independent of the pinhole diameter), and were

repeated using 140 keV photons to model imaging with technetium-99m. The simulations with

iodine-125 were repeated to reduce variability in the data resulting from the reduced photon

135   statistics due to photon attenuation, and the reported results are the average of the two sets of

simulations.

To determine the influence of scatter we derived an additional projection data set by

including only the unscattered photons from the simulations described above to create "scatter-

free" projection data. The scatter-free projection data were reconstructed (with and without

140   attenuation correction) using parameters described below, and the voxel values in the VOI

corresponding to the source were calculated.

The effect of partial volume errors was studied by simulating the imaging of a series of spherical sources with radii varying from 0.5 to 5 mm, with the concentration of radioactivity in the sources kept constant at 2000 Bq/mm^3. The sources emitted 140 keV photons, and the emission angle of the photons was constrained to 0.5π of solid angle to reduce the computation time. A total of 64 projections (30 s/projection) over 360 degrees were simulated. Both the 1 mm and 2 mm pinhole apertures were simulated to assess the effect of pinhole size on partial volume errors, as the spatial resolution (and thus partial volume errors) are strongly influenced by the pinhole size. The simulation did not have any photon attenuation in the source (*i.e.*, the sources were in air) or background activity, which allowed us to evaluate the partial volume effect independently of other factors that may affect the quantitative accuracy. Iodine-125 was not studied in this simulation, because the spatial resolution and thus partial volume errors are not significantly affected by changing isotopes from technetium-99m to iodine-125, as demonstrated for a 1 mm pinhole by McElroy *et al* (McElroy, MacDonald *et al*. 2002). In addition, the effective pinhole diameter calculated for a 1 mm knife-edge pinhole is 1.00 mm and 1.03 mm for iodine-125 and technetium-99m, respectively (Cherry, Sorenson *et al*. 2003) showing that there is minimal change in the amount of septal penetration between these two isotopes. The simulated projection data were reconstructed as described below, and the change in apparent radioactivity as a function of source size was measured by calculating the mean voxel values in a VOI corresponding to the spherical source.

Additional simulations were performed to assess the effects of partial volume errors due to the presence of background radioactivity. A cylindrical source emitting 140 keV photons was simulated with a radius of 1 cm radius and height of 3 cm. The source was aligned with the axis of rotation and centered on the plane defined by the pinhole orbit. The SPECT projection data

165 were simulated without photon attenuation and scatter with a total of 64 projections over 360

degrees. The projection data obtained from the cylindrical source then were added to projection

data obtained using the smaller spherical sources to create sets of projection data for spherical

target sources within a cylindrical background source. Data sets with target to background ratios

of 5:1 and 10:1 were created in this manner.

170 **C.   Experimental measurements**

Experimental measurements were performed using the X-SPECT SPECT/CT scanner

described above. Data were obtained using hollow microsphere phantoms (Data Spectrum, Inc.,

Hillsborough, NC) filled with ^{99m}Tc-NaTcO$_4$ (Table 2). The amount of radioactivity in the

spheres was measured using a dose calibrator (AtomLab 100, Biodex Medical Systems, Shirley

175 NY) prior to imaging. Technetium-99m was chosen for the experimental measurements due to

its low cost and short half-life, which made it easy to re-use the phantoms after the radioactivity

had decayed. On the other hand, imaging studies with iodine-125 can be difficult because it has

a long half-life and iodide ions in solution can react to form ^{125}I-I$_2$, which is volatile, making this

isotope difficult to handle and decontaminate when spills occur. For example, safety regulations

180 at our institution require that iodine-125 be handled in a fume hood and that iodine-125 users

receive regular bioassays.

To study the effect of photon attenuation, the 0.25 mL hollow microsphere was filled with

^{99m}Tc-NaTcO$_4$ and imaged in the X-SPECT scanner. The sphere was placed in a fillable

cylindrical polycarbonate phantom with an outer diameter of 3.2 cm (Figure 2), and imaged with

185 and without water in the surrounding cylinder. 64 projections were acquired over 360 degrees

with a 4 cm radius of rotation using the 1 mm pinhole collimator (data were not acquired with

the 2 mm pinhole for this part of the study because the effects of photon attenuation and scatter

are independent of the pinhole size). After SPECT data acquisition was completed, CT data were acquired using the parameters in Table 3 to generate an attenuation map.

190   To study the effect of partial volume errors on quantitative measurements, microspheres of differing sizes (Table 2) were filled with ^{99m}Tc-NaTcO$_4$ and imaged in the X-SPECT scanner. SPECT data were acquired at 64 projections over 360 degrees, and acquired using both the 1 mm and 2 mm pinhole apertures.

D.   Data reconstruction and analysis

195   Simulated and experimental projection data were reconstructed using various implementations of the ordered subsets-expectation maximization (OS-EM) algorithm using a ray-based projector-backprojector pair (Shepp and Vardi 1982; Lange and Carson 1984; Gullberg, Tsui *et al*. 1990; Zeng and Gullberg 1990). Our implementation used 8 subsets, and data were reconstructed using 5 iterations of this algorithm.

200   One variation of the algorithm included photon attenuation correction (AC), which was performed by modeling the photon attenuation process in the forward and back projectors of the reconstruction algorithm using an attenuation map. For simulated data, the attenuation map was generated using the known geometry of the simulated phantom. In experimental measurements, the attenuation map was created from x-ray CT image data by rescaling the CT images on a

205   voxel-by-voxel basis (Hwang and Hasegawa 2005), and then resampling the data to match the SPECT image matrix. This was shown to qualitatively improve reconstructed SPECT images by reducing artifacts due to photon attenuation (Hwang, Taylor *et al*. 2006).

Data also were reconstructed using an implementation of the OS-EM algorithm which used a realistic model for the collimator (*i.e.*, modeled the finite, position dependent spatial resolution

210   of the pinhole), instead of the ideal pinhole model where the pinhole is treated as an infinitely

small hole in an infinitely thin material. The collimator response was modeled by creating 256

rays (*i.e.*, intersecting the region around the pinhole in a 16x16 array) from each detector pixel,

the path of each ray through the collimator aperture and imaging matrix was then calculated, and

the rays were weighted to account for attenuation in the collimator material (Hwang 2006). The

215   collimator response (CR) model was also combined with a model of photon attenuation to model

both collimator response and photon attenuation in a single reconstruction algorithm. Therefore,

a total of four variations of the OS-EM algorithm were implemented and used: 1) OS-EM

without any corrections, 2) OS-EM modeling photon attenuation, 3) OS-EM with collimator

response modeling, and 4) OS-EM modeling both collimator response and photon attenuation.

220   The qualitative effect of including collimator response in the reconstruction algorithm was

evaluated using a "hot rod" resolution phantom, consisting of radionuclide-filled cylindrical

holes with equal diameter and spacing. The outer diameter of the phantom is approximately 2.5

cm and the rods range in diameter from 1.2 mm to 1.7 mm in 0.1 mm increments. This phantom

was made by and provided to our laboratory by Dr. Nils Schramm (Jülich, Germany). The hot

225   rod phantom was filled with ^{99m}Tc-NaTcO$_4$, and then imaged with the X-SPECT scanner.

Projection data were acquired using a radionuclide detector fitted with a pinhole collimator

having a 2 mm diameter aperture. Data were acquired using a radius of rotation of 3.5 cm at 128

angles over 360° with approximately 9.5×10^4 counts per angular view. The acquisition was

repeated using the 1 mm pinhole aperture using the same parameters, with only approximately

230   4.4×10^4 counts per angular view, due to the reduced detection efficiency of the smaller pinhole

opening. These data were used to estimate the optimum number of iterations to use for image

reconstruction.

        The reconstructed data then were displayed using AMIDE (The Free Software Foundation,

Inc., Boston, MA), an open-source image display and analysis software (Loening and Gambhir

235   2003). A VOI with the nominal geometry of the source was created, and the mean voxel value in

the VOI calculated. For data reconstructed from simulation results, the VOI was placed at the

known location of the source. For experimental data, the VOI was manually positioned to best

overlap the source. To determine the effect of photon attenuation, the mean VOI values were

normalized to the result obtained without any attenuation and then plotted as a function of the

240   radius of the cylinder of water surrounding the simulated source. To study the effect of partial

volume errors, the mean voxel values in the VOI were normalized to the result obtained with a

250 µL source and then plotted as a function of the radius of the simulated radioactive source.

In the experimental data, we found that some radioactivity was present in the "stalk" of the

microsphere, so the mean activity in the sphere was corrected using the following equation:

$$A_{corr} = A_{total} \cdot (1 - \frac{\sum_{stalk} x_i}{\sum_{all\_voxels} x_i}) \tag{1}$$

245   where A_{corr} is the corrected radioactivity, A_{total} is the total measured radioactivity introduced into

the phantom, and the summations represent the sum of the voxel values in the stalk VOI and the

whole reconstructed image, respectively.

III.   RESULTS

A.   Evaluation of reconstruction with collimator response

250   The projection data acquired using the hot rod resolution phantom were reconstructed using

OS-EM with and without geometric compensation for collimator response. The results

demonstrate that incorporating collimator response in the reconstruction algorithm improves

spatial resolution at the expense of requiring more iterations of the algorithm (Figure 3) and thus

increased computation time. We chose to use 20 iterations when reconstructing data using OS-

255   EM with collimator response compensation, and 5 iterations when reconstructing data using OS-EM without collimator response compensation, because the phantom data showed that using more iterations did not substantially improve spatial resolution without collimator response compensation. We found that modeling collimator response in the reconstruction algorithm also improved the spatial resolution of images reconstructed from data acquired with the 1 mm

260   pinhole aperture, but that the improvement is smaller than with data acquired using the 2 mm pinhole aperture.

B.   Monte Carlo simulations

The effect of photon attenuation on quantitative measurements of radioactivity can be demonstrated by plotting the measured radioactivity in the volume of interest as a function of the

265   radius of the surrounding cylinder (Figures 4 and 5 for iodine-125 and technetium-99m, respectively). The results show that photon attenuation causes the radioactivity in the target volume to be underestimated by as much as approximately 50% when imaging iodine-125 in a rat sized object (*i.e.*, 2 cm object radius). When imaging technetium-99m in a rat sized object, photon attenuation reduce the measured target radioactivity by as much as 25%. The results also

270   demonstrate that adding attenuation correction to the reconstruction algorithm will quantitatively compensate for the effect of photon attenuation.

The results obtained with iodine-125 with corrections for both collimator response and photon attenuation overestimate the radioactivity content in the target by 10-20% (Figure 4), which we believe was due to photon scatter. To evaluate the effects of photon scatter, Monte

275   Carlo generated scatter-free projection data simulations were reconstructed. The mean voxel values in the VOI (Figure 6) from these measurements show that scatter contributes to an overestimation of the amount of radioactivity by up to approximately 10%. The scatter-to-

12

primary ratio can be calculated from the number of scattered photons divided by the number of

unscattered photons detected from the Monte Carlo simulations described above for a spherical

280   source inside a cylinder of water. When plotted as a function of the radius of the cylinder, these

results show that the scatter-to-primary ratio can reach approximately 30% in a rat sized object

(Figure 7).

The effect of partial volume errors were analyzed by plotting the average voxel value in the

volume as a function of the radius of the source (Figure 8). The results are normalized to the

285   result obtained with a 250 uL sphere, for which the partial volume errors should be minimal.

These measurements show that smaller sources, particularly those imaged with the 2 mm

pinhole, suffer larger partial volume errors and therefore have a lower measured concentration of

radioactivity than larger spheres. Reconstructing the data using OS-EM with collimator response

helps compensate for the effect of the larger pinhole and thereby reduces partial volume errors to

290   a level comparable to that obtained with the 1 mm pinhole.

The measured radioactivity value was plotted as a function of source size in the presence of

background radioactivity (Figure 9).   These results show that the presence of background

radioactivity will influence the measured radioactivity in the VOI, particularly for smaller

volumes.   In general, the presence of background radioactivity increases the measured

295   radioactivity in the volume of interest, due to "spill-in" caused by the finite spatial resolution.

However, in the case of data acquired with the 2 mm pinhole and reconstructed with an OS-EM

algorithm including collimator response, the presence of background radioactivity causes the

measured radioactivity in the VOI to be underestimated in comparison to the case where

background activity is absent, particularly in the smaller target volumes. This can be seen in

300   Figure 9, where the presence of background radioactivity decreases the value measured within

13

the volume of interest when the data are reconstructed using collimator response. Conversely, the results shown in Figure 9 that are not reconstructed with collimator response show the expected result, where "spill-in" increases the measured value within the VOI for small targets. The unexpected result obtained when reconstructing data with OS-EM incorporating collimator

305 response modeling effect results from the nonlinear behavior of the reconstruction algorithm (Du, Tsui *et al*. 2005), where the tomogram obtained by reconstructing the projections of the target region (T) within a background (B) is not equivalent to summing the tomogram obtained by reconstructing the projections of the target region with the tomogram obtained by reconstructing the projections of the background region. This can be expressed mathematically

310 by the following equation:

$$\text{Rec}[\text{Proj}(T+B)] \neq \text{Rec}[\text{Proj}(T)] + \text{Rec}[\text{Proj}(B)] \tag{2}$$

where $\text{Proj}(x)$ represents the forward projection process, $\text{Rec}(x)$ is the reconstruction process, T is the target volume, and B is the background. This nonlinear behavior is most evident when data acquired with the larger pinhole are reconstructed with collimator response compensation (*i.e.*, resolution recovery) (Pan, Luo *et al*. 1997). Because of this nonlinearity, we did not observe the

315 expected result where spill-in from the background region increases the measured radioactivity concentration in the target volume. In addition, the presence of background radioactivity slows the convergence of the reconstruction algorithm (*i.e.*, more iterations are needed to reach the final value), especially for smaller volumes of interest (Figure 10). These effects complicate the correction of partial volume errors in situations where there is significant background activity.

320 **C.   Experimental measurements**

The results of the experimental measurement on the effect of photon attenuation are shown in Figure 11 by plotting the mean voxel value in the VOI as a function of the product of the

radioactivity in the sphere with the imaging time (which represents the number of disintegrations per volume). As expected, the data fall on a straight line. A least-squares linear fit with the

325 intercept forced to zero was performed for the data acquired without water in the outer cylinder, and a similar fit was performed on data acquired with the outer cylinder filled with water. The slopes of the lines were 1.44 and 1.73, for the cases with and without attenuation, respectively. The discrepancy in the slopes results from the effect of photon attenuation, and indicates that photon attenuation causes the radioactivity concentration to be underestimated by 17% in this

330 particular phantom geometry, consistent with a simple calculation of the attenuation of photons through the phantom. When the data were reconstructed with attenuation correction, the data acquired from the air-filled and water-filled cylinders fell on essentially the same line (slopes of 1.83 and 1.81, respectively), demonstrating that attenuation correction compensates for the effect of photon attenuation with high quantitative accuracy.

335 To study partial volume errors, the mean voxel values in the VOIs from various sized spheres were plotted as a function of the product of the mean activity concentration and the acquisition time, and were normalized by the equivalent values by a large (250 µL) sphere. For each sphere size (31, 63, 125, 250 µL), a least-squares linear fit was performed with the intercept forced to zero. The line fit to the data can be regarded as a calibration curve, where the inverse of the

340 slope gives the value of the scaling factor needed to convert the image voxel values into the absolute concentration of radioactivity multiplied by the imaging time (or radioactive decays per volume). The differences in the slopes for spheres of different sizes reflect the effect of the sphere size on the measured radioactivity due to partial volume errors. Specifically, the slopes are lower for the smaller spheres (Tables 5 and 6), reflecting that the image values for a given

345 amount of radioactivity are decreased due to partial volume errors when imaging smaller

spheres.

D.   Photon scatter

As shown in Figure 7, the scatter-to-primary ratio for imaging mice or rats with iodine-125 can reach 30% or more, which is unexpectedly high, though still lower than the scatter-to-primary ratio typically encountered in human imaging with technetium-99m. However, this result can be explained by examining the contribution of various mechanisms to the linear attenuation coefficient of water. First, the iodine-125 data were acquired with an energy window from 10 to 50 keV (-63.6% to +81.8% of the simulated photopeak energy of 27.5 keV), following the manufacturer's recommendations. This wide energy window is specified to optimize detection efficiency but is not necessarily optimal for quantitative measurement of iodine-125. Furthermore, the Compton component of the linear attenuation coefficient is higher at 27.5 keV than it is at 140 keV (Table 4). Additionally, Rayleigh (coherent) scatter becomes significant at these low energies, and can account for approximately 20% of the total scatter. Rayleigh scatter has a smaller effect on image quality than Compton scatter because of the smaller scatter angles, but can not be rejected using energy discrimination. These factors, combined with the decrease in primary photons due to attenuation, explain the high scatter-to-primary ratio obtained with iodine-125.

We found that Compton scatter during the imaging of rodents with technetium-99m to be negligible (scatter-to-primary ratio less than 10%). The technetium-99m data were acquired using an energy window from 126 to 161 keV (-10% to +15% of the photopeak energy of 140 keV). The lower scatter-to-primary ratio for technetium-99m reflects both the narrower energy window and the lower probability of scatter for technetium-99m versus iodine-125.

16

E.   Comparison of experimental and simulation results

We compared the results of the experimental measurements with the results obtained from
the Monte Carlo simulations in order to verify the simulations results. We first examined the
effect of photon attenuation. The data shown in Figure 11 demonstrate the change in measured
radionuclide concentration in a small source when placed in a water-containing cylindrical
container, which models the measurement of radionuclide uptake in a small tumor within the
torso of a mouse-sized animal. As expected, the radioactivity measured from the image is lower
than the actual source radioactivity due to photon attenuation introduced by the water-equivalent
material surrounding the source. The results show that photon attenuation due to 1.5 cm of water
surrounding a technetium-99m target reduces the apparent radioactivity by almost 20%
compared to the data acquired without the surrounding material, which is similar to the result
predicted by the Monte Carlo simulation (Figure 5). The results also demonstrate that using CT
data for iterative reconstruction based attenuation correction is a quantitatively accurate method
for compensating for the effect of photon attenuation.

A discrepancy between the measured data and the expected results can be seen in the graph
on the right side of Figure 12, where the apparent radioactivity in the largest sphere is actually
slightly lower than the apparent radioactivity in the second and third largest spheres, although we
expect the smaller spheres to have slightly lower apparent radioactivity due to the partial volume
effect. We investigated and found that this deviation could be attributed to count rate effects.
These effects are due to limitations in the rate at which gamma camera electronics can process
signals, resulting in the loss of "counts" when imaging objects containing large amounts of
radioactivity, thereby causing the amount of radioactivity in the sphere to be underestimated
when imaging at high event rates. To measure the count rate limitation of the gamma camera,

17

projection data were acquired using a 250 µL microsphere containing technetium-99m. The gamma camera was fitted with a 2 mm pinhole aperture, and the phantom placed approximately 4 cm from the pinhole. Data were acquired over a period of approximately 2 days in order to allow the technetium-99m in the phantom to decay, thus decreasing the amount of radioactivity

395 in the phantom by a factor of approximately 256. It was found that the relationship between the measured count rate and the known radioactivity content was not linear. At high levels of radioactivity, the count rate deviates from a line fitted to the data acquired with low levels of radioactivity. Thus, imaging at high count rates result in a loss of counts, leading to a decrease in the measured radioactivity. This effect is most evident with larger spheres imaged using the 2

400 mm pinhole aperture.

The microsphere data acquired with the 2 mm pinhole in Figure 12 were adjusted to compensate for the effect of count rate, and compared again with Monte Carlo results (Figure 13). The corrected results show a closer agreement to the simulation results than the uncorrected data.

405 The count rate limitation was significant when the radioactivity in the phantom was over approximately 200 MBq. This is a relatively high amount of radioactivity, and is higher than the amounts that we routinely use in small animal imaging (< 37 MBq), although higher amounts have been used in animal experiments in the past (Wu 2001). This level (>200 MBq) of radioactivity was used for phantom studies involving larger microspheres, but the smaller

410 microspheres usually had lower levels of radioactivity due to their smaller volume. In addition, these data were acquired with the 2 mm pinhole aperture with a 4 cm radius of rotation. If the data were acquired using a smaller pinhole or a larger radius of rotation, the reduced detection

efficiency would allow higher levels of radioactivity to be imaged without significant losses due to count rate limitations.

415 **IV. DISCUSSION**

SPECT has been a mainstay of clinical nuclear medicine for over 3 decades where it has maintained an important role in the assessment of cardiovascular disease, cancer, and disorders in the brain, lung, renal system, and other organs. This has been achieved even though SPECT generally produces qualitative, rather than quantitative results. In other words, a physician or 420 other observer inspects the images visually to differentiate normal from abnormal response. In some cases, numbers are extracted from the images to derive relative values of radionuclide uptake that help in establishing the severity or extent of disease. However, clinical SPECT is rarely considered a quantitatively accurate technique that can measure radionuclide concentration in absolute units (*e.g.*, MBq/mL). Indeed, it generally has been believed that SPECT is not 425 capable of absolute quantification of radionuclide concentration, or of the further step of measuring physiological parameters (*e.g.*, myocardial blood flow) in absolute terms, due to physical effects such as photon attenuation, scatter radiation, and partial volume errors. Nevertheless, its use as a qualitative technique has not prevented SPECT from achieving and maintaining an important role in clinical diagnostic studies.

430 However, it is likely that the more recent advent of SPECT as a preclinical tool may refocus attention on the need for quantitative radionuclide imaging. In the laboratory setting, researchers are trying to use the methods of molecular imaging (including microSPECT) to discern biological response and therapeutic effect at levels that arguably are subtler than those needed to identify the presence of disease. Furthermore, results from the laboratory should be quantified in 435 a way that allows them to be recorded, compared, analyzed, and fit to model systems. The use of

small animal SPECT for quantitative measurements in the laboratory setting therefore is expected to extend well beyond those currently demanded for routine medical diagnostic practice.

In this study, we characterized the errors which affect the quantitative measurement of radionuclide using SPECT, specifically photon attenuation, scatter, and partial volume effects. These errors are common to all forms of radionuclide imaging, and are well characterized for clinical SPECT imaging, but have not been assessed for small animal SPECT imaging. In small animal SPECT imaging, the relative magnitudes of the effects are different (*e.g.*, less photon attenuation in small animal imaging) due to the smaller length scales. In addition, iodine-125 is used in small animal imaging (Choong, Moses *et al.* 2005), but not in human imaging, and its relatively low photon energy results in more photon attenuation and Rayleigh scatter compared with the higher energy isotopes more commonly used for clinical SPECT imaging.

We used Monte Carlo simulations to quantify the magnitude of errors due to photon attenuation, scatter, and partial volume effects on quantitative accuracy by simulating the imaging of spheres of different sizes and in water cylinders of different sizes. The results demonstrated that photon attenuation is significant for iodine-125, leading to a 50% decrease in the measured radioactivity in a rat sized object. With higher energy isotopes such as technetium-99m, the effect of photon attenuation is reduced, but still measurable. Photon scatter caused overestimation of the measured radioactivity with iodine-125, but the result was negligible with technetium-99m. We estimated a scatter-to-primary ratio of 30% with iodine-125 in the simulations, but note that the phantom geometry with a small source at the center of the scattering medium represents a worst-case scenario for scatter. We found that partial volume errors were significant, especially for sources with a radius of less than 2 mm. Partial volume

errors were reduced when the data were reconstructed with collimator response compensation in

460   the reconstruction algorithm, and were also reduced when imaged with smaller pinholes.

The results from several experimental measurements agreed fairly well with the results obtained from the Monte Carlo simulation for photon attenuation and partial volume errors with technetium-99m, after correction for count rate limitations in the gamma camera. The experimental data also showed that photon attenuation correction and collimator response

465   correction in the reconstruction algorithm effectively reduced quantitative errors.

We implemented a scatter correction method in the reconstruction algorithm, but did not thoroughly explore the topic for several reasons. The first is that the effect of scatter on quantitative accuracy is relatively small compared to other errors. Secondly, the effect of scatter is highly dependent on the geometry of both the source and the surrounding materials, making it

470   difficult to draw general conclusions from the results. Finally, quantitative errors resulting from scatter cause a slight overestimation of the amount of radioactivity, which tends to be offset by the relatively large errors caused by photon attenuation and partial volume errors, which result in an underestimation of the tracer concentration.

In general, we found that, as expected, photon attenuation and scatter play a much smaller

475   role in small animal imaging than in human imaging. We found that photon attenuation can reduce the measured radioactivity by approximately 50% in a rat sized object when imaging iodine-125. In contrast, errors of 90% due to photon attenuation have been reported for human imaging with technetium-99m (El Fakhri, Buvat *et al*. 2000). On the other hand, partial volume errors are significant, but are dependent on the geometry of the target volume and the spatial

480   resolution of the system. With appropriate corrections for photon attenuation for iodine-125 and for larger volumes of interest, these results indicate that small animal SPECT has the potential to

be very quantitatively accurate, with errors due to physical effects (*e.g.*, photon attenuation) being smaller than errors introduced by biological factors such as respiratory motion and uncertainties about tumor boundaries, consistent with the results of Forrer *et al* (Forrer, Valkema *et al*. 2006). The results presented in this paper represent a first step in quantifying the uncertainties associated with small animal SPECT imaging, and more work will be needed to further validate the quantitative accuracy of SPECT imaging for specific tracers and animal models used in biological research. For example, simulations can be done using anatomically accurate numerical phantoms such as the MOBY phantom (Segars, Tsui *et al*. 2004).

V. CONCLUSIONS

We have estimated the effects of various physical perturbations on the quantitative accuracy of small animal SPECT, and demonstrated that small animal SPECT data are quantitatively accurate for a range of imaging conditions. Advances in spatial resolution, detection efficiency, and reconstruction algorithms will further improve the quantitative accuracy of this method. We used Monte Carlo simulations and experimental measurements to demonstrate the effect of various physical perturbations on the quantitative accuracy of small animal SPECT data. Specifically, we examined the effect of partial volume errors, photon attenuation, and photon scatter since these are the dominant sources of accuracy errors in clinical SPECT, and we expected them to have an effect in small animal SPECT. We found that photon attenuation is significant with iodine-125, and can result in up to 50% errors when imaging in rat sized objects. The amount of scatter is significant (scatter-to-primary ratio of up to 30%) with iodine-125, with a significant (20%) contribution from Rayleigh scatter. With technetium-99m, the effect of photon attenuation will be less than approximately 30%, which is significantly less than the effect of photon attenuation in human imaging. There will also be much less scatter than in

505 human imaging. Partial volume errors can also be significant, resulting in errors of 50% or more when imaging small volumes of interest. We followed well-investigated methods of improving SPECT image quality and quantitative accuracy by evaluating the use of iterative reconstruction algorithms to compensate for partial volume errors and photon attenuation and found that the use of these algorithms decreased the quantitative errors. However, as in clinical imaging, the

510 magnitude of quantitative errors in small animal imaging will be highly dependent on the specifics of the imaging study; system spatial resolution, target geometry, and choice of tracer and radionuclide used in the study all will affect the quantitative accuracy of the result.

ACKNOWLEDGMENTS

REFERENCES

Agostinelli, S., J. Allison, *et al*. (2003). "Geant4--a simulation toolkit." <u>*Nucl. Instrum. Meth. Phys. Res. A.*</u> **506**(3): 250-303.

Allison, J., K. Amako, *et al*. (2006). "Geant4 developments and applications." *IEEE Trans. Nucl. Sci.* **53**(1): 270-278.

Bennink, R. J., J. Hamann, *et al*. (2005). "Dedicated pinhole SPECT of intestinal neutrophil recruitment in a mouse model of dextran sulfate sodium-induced colitis." *J. Nucl. Med.* **46**(3): 526-31.

Booij, J., K. de Bruin, *et al*. (2002). "Imaging of dopamine transporters in rats using high-resolution pinhole single-photon emission tomography." *Eur. J. Nucl. Med. Mol. Imag.* **29**(9): 1221-4.

Cherry, S. R., J. A. Sorenson, et al. (2003). *Physics in Nuclear Medicine.* Philadelphia, Elsevier Science.

Choong, W.-S., W. W. Moses, *et al*. (2005). "Design for a high-resolution mouse SPECT system using pixellated Si(Li) detectors for in vivo ^{125}I imaging." *IEEE Trans. Nucl. Sci.* **52**(1): 174-80.

Du, Y., B. M. W. Tsui, *et al*. (2005). "Partial volume effect compensation for quantitative brain SPECT imaging." *IEEE Trans. Med. Imag.* **24**(8): 969-976.

El Fakhri, G., I. Buvat, *et al*. (2000). "Relative Impact of Scatter, Collimator Response, Attenuation, and Finite Spatial Resolution Corrections in Cardiac SPECT." *J. Nucl. Med.* **41**(8): 1400-1408.

Forrer, F., R. Valkema, *et al*. (2006). "In vivo radionuclide uptake quantification using a multi-pinhole SPECT system to predict renal function in small animals." *Eur. J. Nucl. Med. Mol. Imag.* **33**(10): 1214-7.

Gullberg, G. T., B. M. W. Tsui, *et al*. (1990). "Estimation of Geometrical Parameters and Collimator Evaluation for Cone Beam Tomography." *Med. Phys.* **17**(2): 264-272.

Hwang, A. B. (2006). *Quantitative Imaging in Small Animals Using SPECT-CT.* <u>Ph.D. dissertation</u>, University of California San Francisco.

Hwang, A. B. and B. H. Hasegawa (2005). "Attenuation correction for small animal SPECT imaging using x-ray CT data." *Med. Phys.* **32**(9): 2799-2804.

Hwang, A. B., C. C. Taylor, *et al*. (2006). "Attenuation correction of small animal SPECT images acquired with ^{125}I-Iodorotenone." *IEEE Trans. Nucl. Sci.* **53**(3): 1213-1219.

Lange, K. and R. Carson (1984). "EM reconstruction algorithms for emission and transmission tomography." *J. Comput. Assist. Tomog.* **8**(2): 306-316.

Loening, A. M. and S. S. Gambhir (2003). "AMIDE: A free software tool for multimodality medical image analysis." *Molec. Imag.* **2**(3): 131-137.

McElroy, D. P., L. R. MacDonald, *et al*. (2002). "Performance evaluation of A-SPECT: a high resolution desktop pinhole SPECT system for imaging small animals." *IEEE Trans. Nucl. Sci.* **49**(5): 2139-2147.

Meikle, S. R., P. Kench, *et al*. (2005). "Small animal SPECT and its place in the matrix of molecular imaging technologies." *Phys. Med. Biol.* **50**(22): R45-61.

Pan, T.-S., D.-S. Luo, *et al*. (1997). "Influence of OSEM, elliptical orbits and background activity on SPECT 3D resolution recovery." *Phys. Med. Biol.* **42**(12): 2517-2529.

565   Santin, G., D. Strul, *et al*. (2003). "GATE: A Geant4-based simulation platform for PET and SPECT integrating movement and time management." *IEEE Trans. Nucl. Sci.* 1516-1521.

Segars, W. P., B. M. Tsui, *et al*. (2004). "Development of a 4-D digital mouse phantom for molecular imaging research." *Mol. Imag. Biol.* **6**(3): 149-59.

570   Shepp, L. A. and Y. Vardi (1982). "Maximum Likelihood Reconstruction for Emission Tomography." *IEEE Trans. Med. Imag.* **M1-1**(2): 113-122.

Strul, D., G. Santin, *et al*. (2003). "GATE (Geant4 Application for Tomographic Emission): a PET/SPECT general-purpose simulation platform." *Nucl. Phys. B.* (*Proc. Suppl.*) **125**: 75-79.

575   Van Laere, K. and H. Zaidi (2006). Quantitative analysis in functional brain imaging. *Quantitative Analysis in Nuclear Medicine Imaging*. H. Zaidi. New York, Springer Science+Business Media, Inc**:** 435-459.

Wu, M. C. (2001). *Development and Application of a High-Resolution Nuclear Medicine Imaging System.* Ph.D. dissertation, University of California San Francisco and 580   University of California Berkeley.

Zeng, G. L. and G. T. Gullberg (1990). "A study of reconstruction artifacts in cone beam tomography using filtered backprojection and iterative EM algorithms." *IEEE Trans. Nucl. Sci.* **37**(2): 759-767.

Zhou, R., D. H. Thomas, *et al*. (2005). "In vivo detection of stem cells grafted in infarcted rat 585   myocardium." *J. Nucl. Med.* **46**(5): 816-22.

FIGURES AND TABLES

590   **Tables**

Table 1: Simulated energy resolution and energy windows for Monte Carlo simulations

	I-125	Tc-99m
Simulated source energy	27.5 keV	140 keV
Energy resolution (%FWHM)	26%	12%
Energy window	10-50 keV	126-161 keV

Table 2: Dimensions of microspheres

Sphere Volume (µL)	Outside Diameter (mm)	Inside Diameter (mm)
250	9.86	7.86
125	8.23	6.23
62.5	6.95	4.95
31.3	5.95	3.95

Table 3: X-ray CT acquisition parameters for microsphere experiments

Parameter	Value
Source to detector distance	298 mm
Detector to center of rotation distance	73 mm
x-ray tube voltage	50 kVp
x-ray tube current	0.6 mA
Number of projections	256

Table 4: Linear attenuation coefficient for water

Photon energy (keV)	Rayleigh Scattering (cm^{-1})	Compton scattering (cm^{-1})	Photoelectric absorption (cm^{-1})	Total attenuation (cm^{-1})
27.5	0.0541	0.182	0.194	0.430
140	0.0028	0.150	0.0009	0.154

Table 5: Slope of voxel value vs. (radioactivity concentration $\times$ imaging time) as a function of source size for data acquired with the 1 mm pinhole

Sphere Volume (μL)	Slope normalized to 250 μL sphere (w/o CR)	Slope normalized to 250 μL sphere (w/ CR)
31	0.85	0.85
63	0.92	0.96
125	0.99	1.01
250	1.00	1.00

Table 6: Slope of voxel value vs. (radioactivity concentration $\times$ imaging time) as a function of source size for data acquired with the 2 mm pinhole

Sphere Volume (μL)	Slope normalized to 250 μL sphere (w/o CR)	Slope normalized to 250 μL sphere (w/ CR)
31	0.70	0.88
63	0.90	1.02
125	0.90	1.00
250	1.00	1.00

Figure Captions

595

Figure 1: Simplified pinhole imaging geometry used for simulations. (a) Detailed view of the pinhole aperture corresponding to the area in the dashed box in the right hand image. (b) Simplified geometry used for the Monte Carlo simulations.

Figure 2: Fillable phantom used in imaging studies (left) Micro Hollow Sphere Set, (Data Spectrum, Inc.). From left to right, the nominal volumes are 31.3, 62.5, 125, and 250 μL. (right) The micro-sphere phantom was mounted in the center of the phantom, which could be filled with water. The outer diameter of the phantom was 3.8 cm.

Figure 3: SPECT images of the hot rod phantom reconstructed using OS-EM with and without collimator response (CR). Data were acquired using 1 mm and 2 mm pinhole apertures using a 3.5 cm radius of rotation and technetium-99m.

Figure 4: Simulated effect of photon attenuation on measured radioactivity in a volume of interest. The average voxel value in the VOI corresponding to the simulated iodine-125 source is plotted as a function of the radius of the water cylinder surrounding the source. The results are normalized to the value obtained in the absence of photon attenuation and demonstrate that attenuation correction improves the quantitative accuracy of the result by compensating for the effect of the water surrounding the source. The data were reconstructed with and without attenuation correction (AC), and also with collimator response modeling (CR). Each data point represents the average value obtained from two simulations.

Figure 5: Simulated effect of photon attenuation on technetium-99m images. Voxel values in the volume of interest are plotted as a function of the radius of the cylinder of water around the source. Data were reconstructed using OS-EM, with and without attenuation correction (AC) and collimator response (CR).

Figure 6: Plot of voxel values in the VOI as a function of the amount of water around the source for iodine-125. Data were reconstructed with all photons detected within the energy window, and again using only unscattered photons. The results show that photon attenuation decreases the measured radioactivity of the source, which is compensated by using attenuation correction (AC). The effect of attenuation is overcompensated due to scatter, causing the mean voxel values in the region of interest to be greater than 100%. The effect of the scatter was demonstrated by reconstructing the data using only unscattered (primary) photons, which eliminates the overcompensation.

Figure 7: Scatter-to-primary ratio for simulated iodine-125 and technetium-99m sources located at the center of a cylinder of water. Increasing the size of the cylinder increases the scatter-to-primary ratio. The energy resolution and energy windows for the simulation are shown in Table 1.

Figure 8: Effect of partial volume errors on the measurement of radioactivity in the volume of interest. The data are from simulated data for a 1 mm pinhole (left), and 2 mm pinhole (right). The mean voxel value in the VOI corresponding to the source is plotted as a function of the radius of the source. The results are normalized to the value obtained with a 250 uL source.

Figure 9: Effect of background radioactivity on voxel values in the volume of interest. The normalized VOI values are plotted as a function of target size for simulated data generated with a 1 mm pinhole (top row) and the 2 mm pinhole (bottom row). Background radioactivity was added, with background to target ratios of 1:10 and 1:5. Data were reconstructed using OS-EM with collimator response (left) and OS-EM without collimator response (right).

Figure 10: The effect of background radioactivity on the convergence of the reconstruction algorithm is shown in this plot. The mean VOI values are shown as a function of iteration number for target spheres with radius of 1 mm and 2 mm with and without background radioactivity, reconstructed using OS-EM with collimator response. The projection data were simulated with a 2 mm pinhole aperture.

Figure 11: Plot of the average voxel value in the VOI for a technetium-99m filled microsphere. The data were acquired with the sphere either in air or in a water filled acrylic cylinder.
(top) Data were reconstructed without attenuation correction, and the difference in the slopes reflects the effect of photon attenuation due to the water in the cylinder on the measurement of radioactivity in the sphere.
(bottom) Data were reconstructed with attenuation correction. The two data sets have essentially the same slope (1.81 and 1.83), demonstrating that attenuation correction compensates for the photon attenuation due to the water in the cylinder.


Figure 12: Plot of the average voxel value in a spherical VOI as a function of the radius of the source (equal to the inner radius of the hollow sphere phantoms for experimental measurements). Data are normalized to the value for a 250 μL VOI. The data are for a technetium-99m source imaged with the (left) 1 mm pinhole aperture, and (right) 2 mm pinhole aperture. For comparison, the results obtained from data generated by Monte Carlo simulation are plotted in the figure (dashed lines) as well. Data were reconstructed using OS-EM with and without collimator response (CR).

Figure 13: Plot of the average voxel value in a spherical VOI as a function of the radius of source (equal to the inner radius of the hollow sphere phantoms for experimental measurements). Data are normalized to the value for a 250 µL VOI. The data are for a technetium-99m source imaged with a 2 mm pinhole aperture, and have been adjusted for the effect of count rate.

Figures
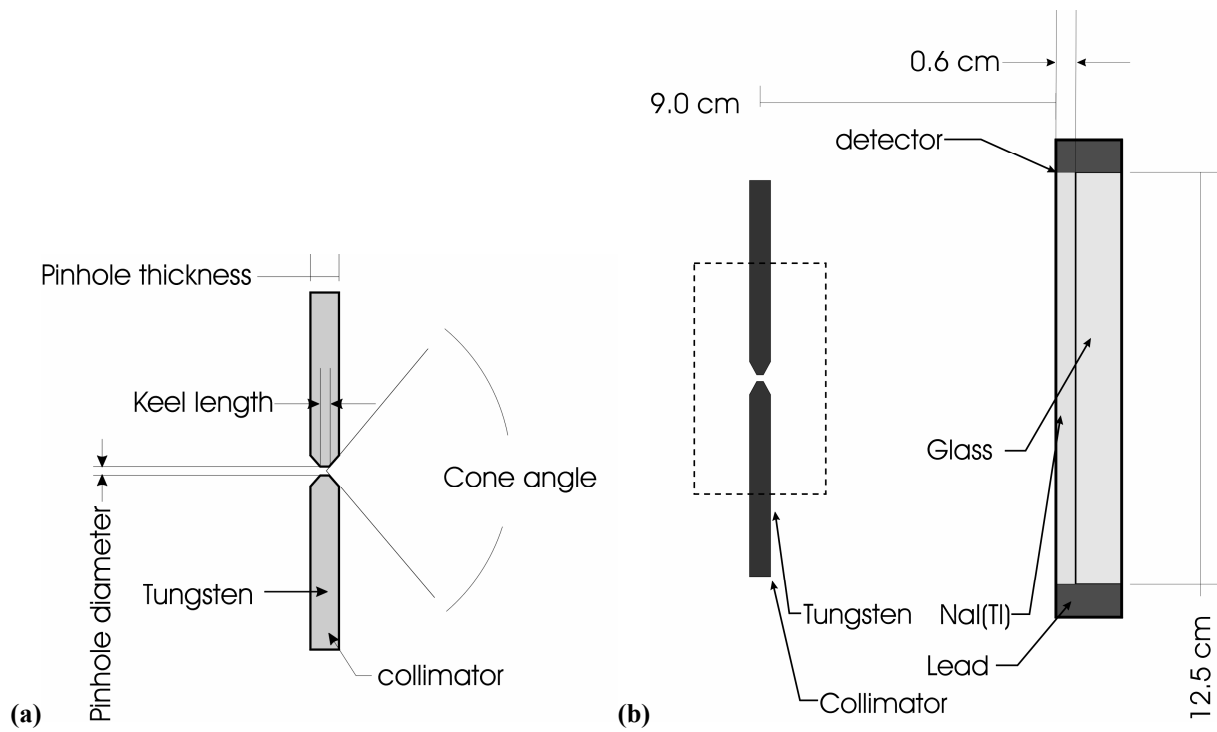
Figure 1: Simplified pinhole imaging geometry used for simulations. (a) Detailed view of the pinhole aperture corresponding to the area in the dashed box in the right hand image. (b) Simplified geometry used for the Monte Carlo simulations.
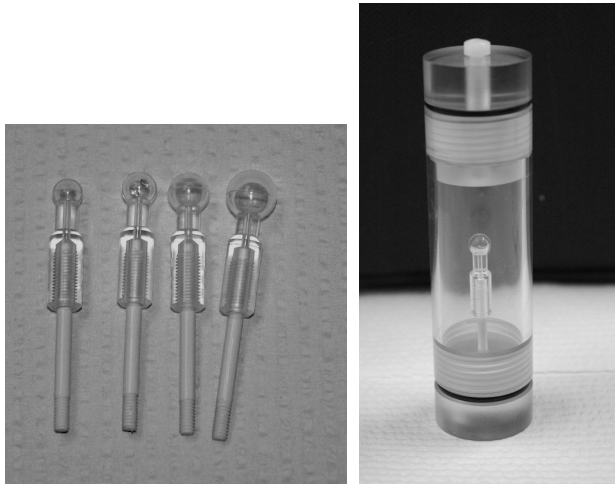
Figure 2: Fillable phantom used in imaging studies (left) Micro Hollow Sphere Set, (Data Spectrum, Inc.). From left to right, the nominal volumes are 31.3, 62.5, 125, and 250 µL. (right) The micro-sphere phantom was mounted in the center of the phantom, which could be filled with water. The outer diameter of the phantom was 3.8 cm.

	Iteration 5	Iteration 10	Iteration 20	Iteration 40	Iteration 60
1 mm PH OS-EM					
1 mm PH OS-EM+CR					
2 mm PH OS-EM					
2 mm PH OS-EM+CR					

Figure 3: SPECT images of the hot rod phantom reconstructed using OS-EM with and without collimator response (CR). Data were acquired using 1 mm and 2 mm pinhole apertures using a 3.5 cm radius of rotation and technetium-99m.

Figure 4: Simulated effect of photon attenuation on measured radioactivity in a volume of interest. The average voxel value in the VOI corresponding to the simulated iodine-125 source is plotted as a function of the radius of the water cylinder surrounding the source. The results are normalized to the value obtained in the absence of photon attenuation and demonstrate that attenuation correction improves the quantitative accuracy of the result by compensating for the effect of the water surrounding the source. The data were reconstructed with and without attenuation correction (AC), and also with collimator response modeling (CR). Each data point represents the average value obtained from two simulations.

Figure 5: Simulated effect of photon attenuation on technetium-99m images. Voxel values in the volume of interest are plotted as a function of the radius of the cylinder of water around the source. Data were reconstructed using OS-EM, with and without attenuation correction (AC) and collimator response (CR).
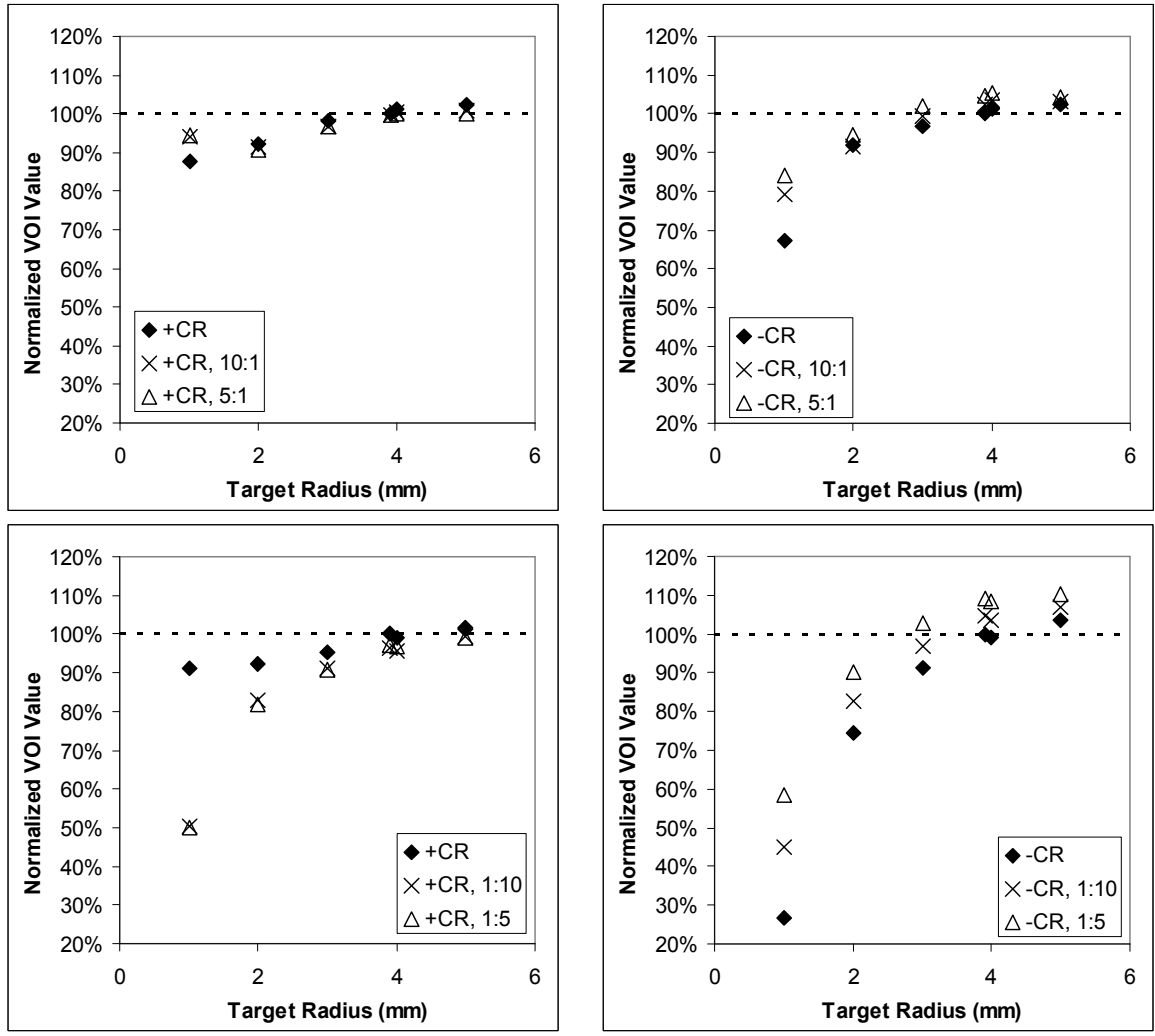
Figure 6: Plot of voxel values in the VOI as a function of the amount of water around the source for iodine-125. Data were reconstructed with all photons detected within the energy window, and again using only unscattered photons. The results show that photon attenuation decreases the measured radioactivity of the source, which is compensated by using attenuation correction (AC). The effect of attenuation is overcompensated due to scatter, causing the mean voxel values in the region of interest to be greater than 100%. The effect of the scatter was demonstrated by reconstructing the data using only unscattered (primary) photons, which eliminates the overcompensation.
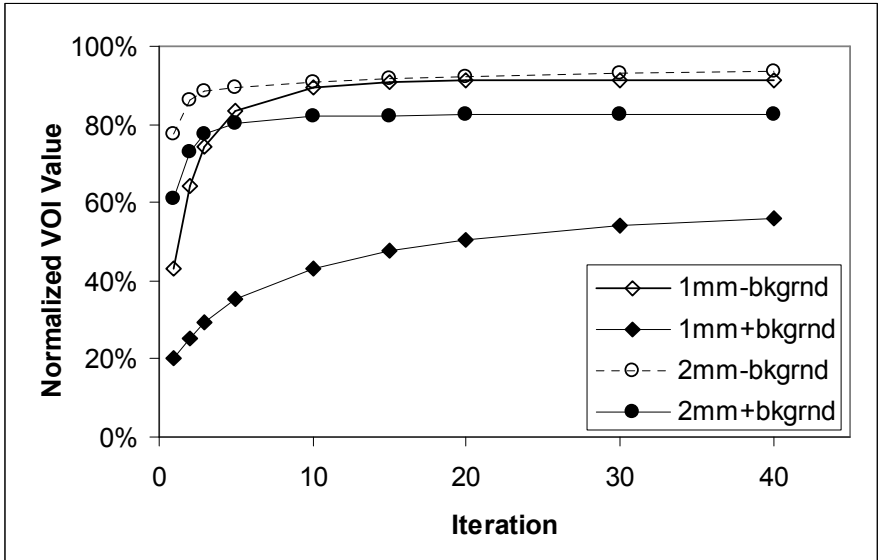
Figure 7: Scatter-to-primary ratio for simulated iodine-125 and technetium-99m sources located at the center of a cylinder of water. Increasing the size of the cylinder increases the scatter-to-primary ratio. The energy resolution and energy windows for the simulation are shown in Table 1.

Figure 8: Effect of partial volume errors on the measurement of radioactivity in the volume of interest. The data are from simulated data for a 1 mm pinhole (left), and 2 mm pinhole (right). The mean voxel value in the VOI corresponding to the source is plotted as a function of the radius of the source. The results are normalized to the value obtained with a 250 uL source.
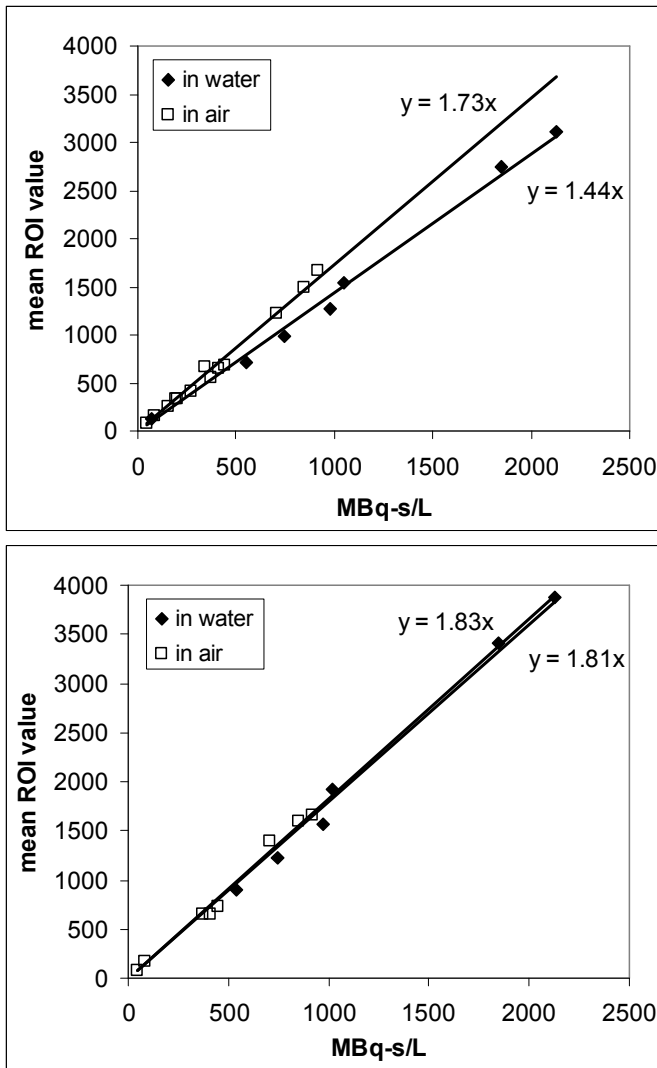
Figure 9: Effect of background radioactivity on voxel values in the volume of interest. The normalized VOI values are plotted as a function of target size for simulated data generated with a 1 mm pinhole (top row) and the 2 mm pinhole (bottom row). Background radioactivity was added, with background to target ratios of 1:10 and 1:5. Data were reconstructed using OS-EM with collimator response (left) and OS-EM without collimator response (right).
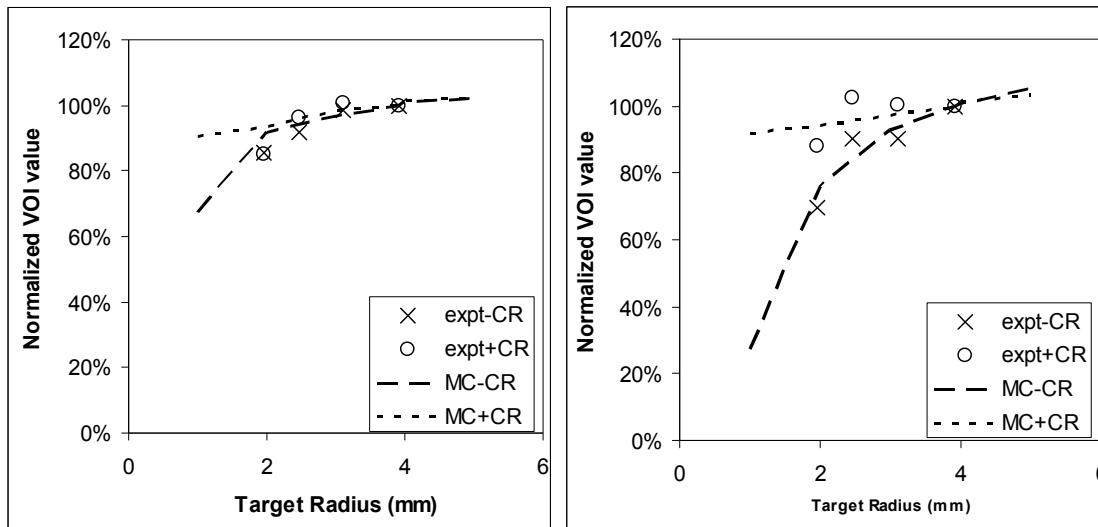
Figure 10: The effect of background radioactivity on the convergence of the reconstruction algorithm is shown in this plot. The mean VOI values are shown as a function of iteration number for target spheres with radius of 1 mm and 2 mm with and without background radioactivity, reconstructed using OS-EM with collimator response. The projection data were simulated with a 2 mm pinhole aperture.
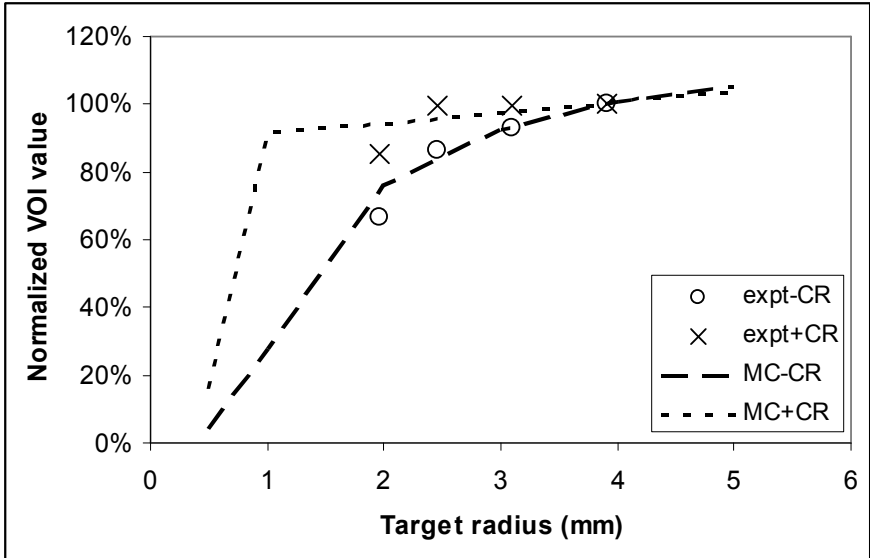
600

Figure 11: Plot of the average voxel value in the VOI for a technetium-99m filled microsphere. The data were acquired with the sphere either in air or in a water filled acrylic cylinder.

(top) Data were reconstructed without attenuation correction, and the difference in the slopes reflects the effect of photon attenuation due to the water in the cylinder on the measurement of radioactivity in the sphere.

(bottom) Data were reconstructed with attenuation correction. The two data sets have essentially the same slope (1.81 and 1.83), demonstrating that attenuation correction compensates for the photon attenuation due to the water in the cylinder.

41

Figure 12: Plot of the average voxel value in a spherical VOI as a function of the radius of the source (equal to the inner radius of the hollow sphere phantoms for experimental measurements). Data are normalized to the value for a 250 µL VOI. The data are for a technetium-99m source imaged with the (left) 1 mm pinhole aperture, and (right) 2 mm pinhole aperture. For comparison, the results obtained from data generated by Monte Carlo simulation are plotted in the figure (dashed lines) as well. Data were reconstructed using OS-EM with and without collimator response (CR).

Figure 13: Plot of the average voxel value in a spherical VOI as a function of the radius of source (equal to the inner radius of the hollow sphere phantoms for experimental measurements). Data are normalized to the value for a 250 µL VOI. The data are for a technetium-99m source imaged with a 2 mm pinhole aperture, and have been adjusted for the effect of count rate.